Replacement of microglia by monocyte-derived macrophages prevents long-term memory deficits after therapeutic irradiation

Xi Feng[1,2], David Chen[1,2,3], Sonali Gupta[1,2], Sharon Liu[3], Nalin Gupta[3,6,7] and Susanna Rosi[1,2,3,4,5*]

[1] Brain and Spinal Injury Center

[2] Department of Physical Therapy and Rehabilitation Science

[3] Department of Neurological Surgery

[4] Weill Institute for Neuroscience

[5] Kavli Institute of Fundamental Neuroscience

[6] Brain Tumor Research Center

[7] Department of Pediatrics

University of California San Francisco

* Corresponding Author

Susanna Rosi Ph.D.: Susanna.Rosi@ucsf.edu

1001 Potrero Ave, Building 1, Room 101, Zuckerberg San Francisco General Hospital
Department of Physical Therapy and Rehabilitation Science, University of California, San Francisco, San Francisco, CA 94110

Running Title:

Keywords: microglia, monocyte, cognition, brain irradiation, CSF-1R inhibitor

Abstract

Resident microglia of the brain have a distinct origin compared to macrophages in other organs. Under physiological conditions, microglia are maintained by self-renewal from the local pool, independent of hematopoietic progenitors. Pharmacologic depletion of microglia during therapeutic whole-brain irradiation prevents synaptic loss and rescues recognition memory deficits but the mechanisms behind these protective effects are unknown. Here we demonstrate that after a combination of therapeutic whole-brain irradiation and microglia depletion, macrophages originating from circulating monocytes engraft into the brain and replace the microglia pool. Comparisons of transcriptomes reveal that brain-engrafted macrophages have an intermediate phenotype that resembles both monocytes and embryonic microglia. Importantly, the brain-engrafted macrophages have a reduced phagocytic activity for synaptic compartments compared to the activated microglia from irradiated brains, which in turn prevent the aberrant and chronic synapse loss that results in radiation-induced memory deficits. These results are the first to demonstrate that replacement of microglia by brain-engrafted macrophages represent a potential therapeutic avenue for the treatment of brain radiotherapy induced cognitive deficits.

Introduction

Microglia are the resident innate immune cells of the central nervous system (CNS). They arise from the yolk sac during embryonic development, and are involved with active surveillance of the environment to maintain normal brain functions [1, 2]. Under physiological conditions, the microglia population is maintained solely by self-renewal from the local pool [3]. Following brain injury and other pathological conditions, microglia became activated and play a central role in the clearance of cellular debris, neuroinflammation and aberrant synaptic engulfment [4-7]. Temporary depletion of microglia can be achieved by using pharmacologic inhibitors of the colony-stimulating factor 1 receptor (CSF-1R) [8]. In the normal brain, treatment with CSF-1R inhibitors can deplete up to 99% of microglia without causing detectable changes to cognitive functions [8, 9]. Full repopulation occurs within 14 days of inhibitor withdrawal and the repopulated microglia are morphologically and functionally identical to the microglia in brains without inhibitor treatment [9]. Microglia depletion and repopulation by local progenitors has been shown to be beneficial for disease- ,injury- , and age-associated neuropathological and behavioral conditions[10-15]. However, the mechanisms for these protective effects are unknown.

Whole-brain radiotherapy (WBRT), delivered in multiple fractions, is routinely used to treat patients with brain tumors. It is estimated that more than 200,000 patients receive WBRT yearly in the US alone [16]. While it is effective in improving intracranial tumor control WBRT leads to deterioration of patients' cognitive functions and quality of life [17-19], and unfortunately, there is no treatment available to prevent or mitigate these adverse effects. Previous studies demonstrated that WBRT causes deleterious effects to the CNS microenvironment by a number of mechanisms including apoptosis of neural progenitor cells, disruption of the blood-brain barrier, activation of microglia and accumulation of peripherally derived macrophages [20-25]. We and others have reported that depletion of microglia during or shortly after brain irradiation in animal models can prevent loss of dendritic spines in hippocampal neurons and cognitive

impairments that develop at later time points [12-14]. These reports suggest that microglial activation plays a critical role in inducing synaptic abnormalities and consequently, cognitive deficits after brain irradiation. The underlying molecular pathways leading to these radiotherapy-induced neuronal alterations remain unknown.

In the current study, we performed a detailed analysis of the transcriptional profile of repopulated microglia isolated by flow sorting from irradiated mouse brains after CSF-1R inhibitor-mediated depletion. We observed that CSF-1R inhibitor treatment alone results in >95% depletion of microglia, followed by full recovery from of this population within 4 weeks, which is consistent with previous reports [8, 9, 12]. However, surprisingly, the microglia present after WBRT originate from peripheral monocytes rather than CNS resident population. These monocyte-derived brain-engrafted macrophages (BEMs) have an intermediate transcriptional signature that resembles both peripheral monocytes and embryonic microglia during development. Notably, the transcriptomic changes induced by therapeutic brain irradiation were fully reset to control levels in the monocyte-derived BEMs. Most importantly, after irradiation the monocytes-derived BEMs had a reduced ability to engulf synaptic compartments compared to brain resident microglia. Brief depletion of microglia at the time of irradiation and repopulation by BEMs permanently prevents the radiation-induced synapse loss and recognition memory deficits. These results uncover: 1) the mechanism by which radiotherapy affect hippocampal synapses and memory functions, 2) the mechanisms by which temporary microglia depletion and repopulation chronically protects synapse and memory loss and lastly, 3) indicate the replacement of microglia by BEMs as a potential treatment for radiation induced memory deficits.

Results

Temporary microglia depletion prevents radiation-induced memory deficits.

Temporary microglia depletion during or shortly after exposure to brain irradiation prevents cognitive deficits, suggesting microglia's key role in modifying neuronal and cognitive functions [12-14]. Changes in expression levels of pro-inflammatory cytokine/chemokines have been shown to correlate with cognitive performance in mice [12, 15, 20], however, the exact change in the transcriptional profile of repopulated microglia after brain irradiation is unknown and is an important tool to dissect the roles that microglia play in the development of radiation-induced memory deficits. We performed RNA sequencing using repopulated microglia, FACS sorted from irradiated and control mouse brains after CSF-1Ri treatment, and compared with transcriptomes of microglia obtained from mice without CSF-1Ri treatment (Figure 1a). A CSF-1R inhibitor was used to fully deplete microglia in 8-weeks old male mice, for a duration of 21 days. Three fractions of therapeutic whole-brain irradiation were given to each mouse every other day over five days starting from day 7 of CSF-1R inhibitor treatment. Novel Object Recognition (NOR) test was used to measure recognition memory 4 weeks after the last fraction of WBRT. Consistent with our previous report, fractionated WBRT resulted in impairment in recognition memory, which was prevented by CSF-1R inhibitor treatment (Figure 1a, lower panel). One day after the NOR test, mice were euthanized and whole brains were used to sort microglia ($CD45^{low}CD11b^{+}$ population) for RNA extraction. In order to maximize discoveries from transcriptomic analyses, we chose samples from the best performers in non-impaired groups (control diet + sham, CSF-1R inhibitor + sham/WBTR) and the worst performers in the memory impaired group (control diet + WBRT) for RNA sequencing (Figure 1a).

Microglia depletion and repopulation eliminates the radiation-induced transcriptome signatures

To identify biological pathways involved in radiation-induced memory deficits, we listed genes differentially expressed in microglia after WBRT for Gene Ontology Biological Process (GOBP) enrichment analysis. Two hundred and four genes were found to be significantly up- or down-regulated only in microglia isolated from irradiated versus naïve brains on Control diet (Figure 1b and Supplementary Table 1). No enriched GOBP terms were found from the 87 WBRT down-regulated genes (Supplementary Table 1). There were 193 enriched GOBP terms from the 117 WBRT up-regulated genes, the top 20 enriched GOBP terms are listed in Figure 1c. Almost half (96) of these enriched GOBP terms were associated with increased response to cell cycle regulation, radiation, DNA repair and stress; the rest enriched GOBP terms were associated with increased metabolism (21), development (12), regulation of protein kinase activity (8), cellular adhesion (4) and other functions (Figure 1d, Supplementary Table 1). These results demonstrate that WBRT was the main driver for the changes measured in the genes and biological pathways. However, the top three enriched GOBP terms (toll-like receptor 3 signaling pathway, adhesion of symbiont to host, and positive regulation of interleukin-6 secretion) were not directly associated with radiation effects, suggesting that an increase of these functions are also linked to memory impairments after WBRT.

qPCR validation of the RNAseq results

To validate the RNAseq results, we next performed qPCR analyses using sorted microglia from animals in the same cohort (see RNAseq results of tested genes in RNAseq in Figure 1b, and Supplementary Table 1). The expression of the toll-like receptor 3 (TLR3) family gene *Lgals9* was significantly increased by irradiation (WBRT + Control diet versus Sham + Control diet), and was at levels comparable to the shams (Sham + Control diet) when treated with CSF-1Ri

despite of irradiation (Figure 2a). *TNFα*, another TLR3 family member which also belongs to GOBP "regulation of response to reactive oxygen species (ROS)", was significantly upregulated by irradiation (WBRT + Control diet versus Sham + Control diet); its expression levels are comparable between the Sham + Control diet and the WBRT + CSF1Ri treated groups. However, *TNFα* remained elevated in microglia from mice treated only by CSF-1Ri (Figure 2b). Another gene from the GOBP "regulation of response to ROS", *Sesn2*, was also significantly upregulated by WBRT (Figure 2c). *Sesn2* remained at the control sham levels in CSF-1Ri only group and was significantly down-regulated in the WBRT + CSF-1Ri group. *Mdm2*, a gene that belongs to GOBP "cellular response to ionizing radiation", was increased after WBRT, and significantly downregulated in in CSF-1Ri treated groups (Figure 2d). Other WBRT-induced expression of radiation induced genes, *Ddias*, *Rad51, FoxM1* and *Check 1*, were all at the control sham levels in repopulated microglia regardless of the exposure to WBRT (Figure 2 d – h). In conclusion, the qPCR validation confirmed that the transcriptomic changes seen in our RNAseq dataset were reliable. These results suggest that CSF-1Ri mediated microglia depletion during WBRT followed by repopulation is able to reset radiation-induced direct effects on the microglia transcriptome.

Repopulated microglia after WBRT originate from peripheral monocytes

Bone marrow transplant (BMT) using whole-body irradiation allows peripheral myeloid cells to enter the brain and contribute to the microglia pool [2, 26, 27]. The fractalkine receptor CX3CR1 is expressed in both microglia and peripheral monocytes [28], while chemokine receptor CCR2 is mainly expressed in monocytes [29]. In the $Cx3cr1^{GFP/+}Ccr2^{RFP/+}$ reporter mice, the different expression patterns of GFP and RFP can be used to distinguish microglia from monocytes [29]. To investigate the cell-of-origin of repopulated microglia in our experimental paradigm we generated bone marrow chimeras with head-protected irradiation using fluorescent labeled bone

marrow from Cx3cr1$^{GFP/+}$Ccr2$^{RFP/+}$ donor mice (Figure 3a). This allowed partial replacement of bone marrow cells without changing the permeability of the blood-brain-barrier. At 6 weeks after bone marrow transplantation about two thirds of peripheral monocytes were replaced by transplanted cells with fluorescent labels (Figure 3b). Bone marrow chimera animals were then treated with CSF-1R inhibitor and WBRT following the same experimental timeline used for RNA sequencing (Figure 3a). Next, we compared the compositions of myeloid cells in the brain after CSF-1R inhibitor-mediated depletion and repopulation. Flow cytometry analyses performed 33 days after WBRT revealed that microglia depletion and repopulation alone (Sham + CSF-1Ri) only resulted in limited accumulation of transplanted cells in the brain (Figure 3c). However, in mice that received WBRT and CSF-1Ri, two thirds of the microglia were replaced by Cx3cr1-GFP labeled cells (Figure 3c). These results suggest that microglia depletion during WBRT results in significant contribution of the CNS microglia pool by peripheral monocyte-derived BEMs. Notably, the percentage of donor derived monocytes in the blood are similar to that of CX3CR1-GFP labeled BEMs, suggesting that the replacement of microglia might be higher than the data shown here (Figure 3c).

Brain-engrafted macrophages retain monocyte signatures

We next determined the transcriptomic signature of the BMEs after microglia depletion and WBRT by comparing our RNAseq dataset with a previous report by Lavin and Winter *et al* [30]. To minimize false discovery and noise signals, we examined 1201 genes from this published dataset with a fold change greater than 1.50 (or smaller than 0.667 for down-regulated genes, $p<0.05$, monocyte compared to naïve microglia), and found that 1066 genes were expressed in our samples (Supplementary Table 2). Strikingly, the hierarchical clustering of 525 monocyte- and 541 microglia-signature genes revealed that the expression profile of monocyte-derived BEMs (WBRT + CSF-1Ri) does not cluster with naïve (Sham + Control diet), irradiated (WBRT

+ Control diet) or repopulated (Sham + CSF-1Ri) microglia (Figure 3d). Similarity matrix analysis revealed that the expression patterns in naïve, irradiated and repopulated microglia were highly similar to each other, while sharing less similarity with BEMs after microglia depletion and WBRT (Figure 3e). Next, we counted genes in each group that expressed in the same trends as microglia or monocyte signature genes from the Lavin set to determine the similarity scores to these two cell populations. We found that, naïve, irradiated and repopulated microglia had 60%, 57% and 51% (718, 685 and 612) genes expressed in the same trends as microglia signature genes, respectively, with minimum similarity (2-3%) to monocyte signature genes; while BEMs expressed both microglia (28%, 331 genes) and monocyte signature genes (32%, 386 genes) (Figure 3f). These results further confirm that after microglia depletion and WBRT BEMs originate from blood monocytes. Interestingly, these BEMs have partial microglia and partial monocyte signatures.

qPCR validation of microglia- and monocyte-specific genes

To validate microglia and monocyte signature genes that were differentially expressed in our RNAseq results we next performed qPCR analyses (Figure 3d and Supplementary Table 2). Microglia signature genes *Sall1*, *P2ry12*, *Tmem119* and *Trem2* were expressed at comparable levels in naïve, irradiated and repopulated microglia, while at significantly lower level in BEMs (Figures 4 a – d). On the other hand, expression of monocyte signature gene *Runx3*, was significantly higher in BEMs than other groups (Figure 4e). Notably, previously reported brain-engrafted macrophage specific genes *Lpar6* and *Pmepa1* [31] have significantly higher expression levels in BEMs after CSF-1Ri and WBRT treatments compared to other groups (Figure 4 f and g). In addition, the expression of *Ccr2*, a monocyte signature gene that was not differentially expressed in our RNAseq dataset, was also not differentially expressed among the four experimental groups by qPCR (Figure 4h). Taken together, these qPCR results validate our

RNAseq results and demonstrate that BEMs after microglia depletion and WBRT originate from peripheral monocytes.

Monocyte-derived brain-engrafted macrophages resemble embryonic microglia signatures

Because monocyte-derived BEMs were exposed to the brain microenvironment for a short period of time, we hypothesized that they were functionally immature. To test this hypothesis, we first examined genes that were highly expressed at different developmental stages in microglia, and used yolk sac/embryonic and adult-specific genes as references (called embryonic and adult signature genes hereon) [32]. Hierarchical clustering of 1617 embryonic and 785 adult microglia signature genes revealed that transcriptomes of BEMs were highly similar to embryonic microglia, while the transcriptomes of microglia from other groups were similar to adult microglia and did not resemble the embryonic one (Figure 5a). In addition, a similarity matrix analysis using all 2402 overlapped genes between two datasets showed that BEMs had the lowest similarity with microglia from other groups (Figure 5b). In addition, 54% of the listed genes (n=1306) in BEMs expressed in the same trends as *yolk sac*/embryonic microglia compared to adult microglia (Figure 5c). In contrast, naïve (Sham), irradiated (WBRT only) and repopulated microglia (CSF-1Ri only) had much lower embryonic signature similarity scores (16%, 19% and 17%, n=381, 445 and 405, respectively, Figure 5c). Notably, naïve, irradiated and repopulated microglia transcriptomes had high adult signature similarity scores (69%, 59% and 63%, n=1649, 1409 and 1507, respectively), while BEMs had the lowest adult similarity score (32%, n=759). These data suggest that the monocyte-derived BEMs start to resemble microglia by first expressing immature microglia signature compared to naïve, irradiated and repopulated microglia.

Microglia depletion during WBRT prevents radiation-induced loss of hippocampal PSD95

We previously demonstrated that brain irradiation resulted in reduced density of dendritic spines in hippocampal neurons [13]. To determine more accurately the effect of WBRT in the intrinsic synaptic protein levels we measured pre- and post-synaptic markers in the hippocampus by flow-synaptometry [33, 34]. Fractionated hippocampal cell membranes containing synaptosomes were enriched and particles between 1 – 3 µm were analyzed to measure synaptic protein levels using mean fluorescent intensities by FACS (Figure 6a). We observed no changes in pre-synaptic Synapsin-1 protein levels in the hippocampi across all groups (Figure 6b). However, we measured a significant reduction in post-synaptic protein PSD-95 after WBRT, which was completely prevented by CSF-1R inhibitor mediated microglia depletion (Figure 6b). These results confirm that microglia plays a key role in the radiation-induced loss of post-synaptic components after WBRT.

WBRT induces aberrant phagocytosis activity in microglia that is abrogated in brain-engrafted macrophages

Aberrant loss of synapses during neuroinflammatory conditions has been linked with increased engulfment of synaptic compartments by microglia [35]. To determine if WBRT affect the phagocytosis potency of microglia, we injected pre-labeled synaptosomes from a naïve donor mouse into the hippocampi of mice after WBRT and CSF-1R inhibitor treatment and measured engulfment of labeled synaptosomes by microglia using flow cytometry (Figure 5a). After WBRT there was a significant increase in the number of microglia engulfing synaptosomes in the hippocampus compared to naïve non-irradiated animals (Figure 7b). Strikingly, synapse engulfment activity was unchanged compared to naïve animals in animals treated with CSF-1R inhibitor during WBRT (Figure 7b). Immunofluorescent imaging at the injection sites confirmed

that the injected synaptosomes were indeed engulfed by microglia, and the increased trend of engulfment by irradiated microglia remained unchanged (Figures 7 c and d, Supplementary Figure 1a). Notably, after hippocampal injection of fluorescent labeled latex beads into the hippocampus, we found that WBRT resulted in increased engulfment of latex beads was also inhibited by CSF-1R inhibitor treatment, suggesting that the WBRT-induced increase of engulfment was not specific to synaptosomes, but rather a general increase of phagocytosis potency (Supplementary Figure 1b). These data are the first to demonstrate that WBRT results in an increase in microglial phagocytosis activity in the hippocampus that can be prevented by transient microglia depletion.

Irradiation-induced expression of complement and phagocytic receptors are prevented by transient microglia depletion

Microglial complement receptors play essential roles in physiologic synaptic elimination during development and aberrant elimination during neuroinflammatory conditions [35, 36]. To understand the mechanisms of increased microglia phagocytic activity after WBRT, we measured expression levels of a list of complement receptors, phagocytic markers and lysosome proteins in microglia by flow cytometry. The expression of complement receptor C5aR was significantly elevated in microglia at one month after WBRT. However, in animals treated with CSF-1Ri C5aR expression was unchanged from naïve animals (Figure 7e). The same trend was observed in the expression levels of CD68 and lysosomal-associated membrane protein 1 (LAMP-1) (Figure 7 f and g). These results were consistent with our data demonstrating decreased PSD95 levels (Figure 4b) and increased microglial phagocytosis activity in the hippocampus after WBRT (Figure 5 b and d). In addition, complement receptor CR3 (CD11b) was significantly elevated in microglia after WBRT or CSF-1Ri treatments alone, and remained unchanged in BEMs with combined WBRT and CSF-1Ri treatments (Supplementary Figure 2a).

No changes in the complement receptor C3ar1 were measured after WBRT or CSF-1R inhibitor treatment (Supplementary Figure 2b). These results demonstrate that the increased microglia phagocytosis of synaptosomes after WBRT was associated with increased phagocytic and lysosome proteins, and was likely through the complement pathways.

Brain-engrafted macrophages persist in the brain and provide long-term protection against WBRT-induced memory deficits and hippocampal dendritic spine loss

To determine whether BEMs are present long-term in the brain, we monitored BEMs for 6 months (Figure 8 a). To eliminate the limitation of using bone marrow obtained from the Cx3cr1$^{+/GFP}$Ccr2$^{+/RFP}$ knock-in reporter mouse strain, we used an actin-GFP transgenic line as bone marrow donors and generated chimeras using the same body-only irradiation protocol (Figure 8 a). Six weeks later, mice were treated with CSF-1R inhibitor and WBRT and then used to trace BEMs at long-term time points (Figure 8 a). Coronal sections at the level of the dorsal hippocampus were stained with Iba1 and imaged to quantify total Iba1+ and GFP+ cells (Supplementary Figure 3 a). We found that all GFP+ cells in the brain were also Iba1+, suggesting that they were indeed BEMs. In addition, the morphology of Iba1+GFP+ BEMs were similar to Iba1+GFP- microglia (Figure 8 b). We observed increased microglia replacement by BEMs at 14 days after WBRT, or 4 days after CSF-1Ri withdrawal, and sustained to 6 months after WBRT (Figure 8 c). To measure the long-term cognitive outcomes, we treated a batch of wildtype animals, and tested their recognition memory at 3 and 6 months after WBRT (Figure 8 d). We found that WBRT resulted in persistent loss of recognition memory also at 3 and 6 months, while CSF-1Ri treatment alone did not alter recognition memory performance (Figure 8 e and f). Strikingly, mice that received WBRT along with temporary microglia depletion did not show any memory deficits and performed undistinguishable from control animals at 3 and 6 months (Figure 8 e and f). Our previous report demonstrated that WBRT-induced dendritic spine

loss in hippocampal neurons was fully prevented by temporary microglia depletion during irradiation (Figure 8 g, replotted using previously published data) [13]. In this study, we sought to understand if the protective effects persisted up to 6 months after WBRT. Our results clearly show that radiation-induced loss of dendritic spines in hippocampal neurons persists to this time point, and that the protective effect of microglia depletion and subsequent replacement by BEMs is long lasting (Figure 8 h). Taken together, temporal depletion of microglia during WBRT induces sustainable BEMs in the brain and provides long-term protection against irradiation-induced deficits in recognition memory.

Discussion

Our results demonstrate that activated microglia following WBRT have an increased potency to engulf synaptic compartments (Figure 7 b – d) which results in persistent synapse loss (Figure 6 b, Figure 8 g and h) and memory impairments (Figure 1 a and Figure 8 e and f). Temporary depletion of microglia during WBRT leads to the accumulation of a functionally distinct cell population in the brain which we described as monocyte-derived BEMs (Figure 3 and Figure 8 a - c). BEMs are characterized by the following features: 1) reset of the WBRT-induced transcriptomic changes associated with cell cycle regulation, DNA damage and stress responsive pathways, and 2) reduced phagocytic activity towards synaptic compartments that prevent irradiation-induced loss of synapses and memory impairments. Importantly, replacement of microglia by BEMs provided long-term protection against hippocampal-dependent memory loss and represent a potential treatment that could protect patients from memory deficits after WBRT.

In the CNS, microglia maintain a stable population by self-renewal in either a random manner or through clonal expansion [3, 37]. CSF-1R inhibitor treatment alone results in acute

depletion of up to 99% of CNS resident microglia, with repopulated microglia arising solely from the residual microglia and their progenitor cells that remain after treatment [8, 38]. The repopulated microglia have transcriptional and functional profiles similar to naïve microglia [9]. Peripheral macrophages can engraft into the brain but remain morphologically, transcriptionally and functionally different from CNS resident microglia [39, 40,]. Under specific circumstances, monocytes entering the CNS can become microglia-like cells. This is most clearly demonstrated in experiments where lethal whole-body irradiation was followed by bone marrow transplantation with labeled monocytes ($Ccr2^{+}Ly6C^{high}$), resulting in accumulation of these cells in the brain [26]. In addition, chronic depletion of microglia without irradiation also results in myeloid cells entering the CNS and becoming BEMs [31]. Here we report that concurrent microglia depletion and therapeutic brain irradiation causes peripheral monocytes to enter the brain parenchyma and become microglia-like BEMs. BEMs enter the brain at 14 days after the completion of brain irradiation, or 4 days after the CSF-1Ri withdrawal, rather than immediately after WBRT (Figure 8 c). These results suggest that prolonged CSF-1Ri treatment after irradiation is able to block the engraftment of BEMs to the brain. Notably, at this time point the total number of Iba1 positive cells is not fully recovered (Supplementary Figure 3 b). Therefore, a small increase in GFP positive cell number results in a noticeable increase in the replacement ratio of microglia by BEMs in irradiated brains compare to non-irradiated brains (Supplementary Figure 3 c and Figure 8 c). This ratio remains at high levels in head-irradiated mice throughout the current study (Figure 8 c), suggesting that microglia depletion during WBRT results in sustainable replacement of microglia by BEMs. Importantly, this observation correlates with long-term protection against WBRT-induced loss of recognition memory and dendritic spines in hippocampal granule neurons (Figure 8 e – h).

Microglia play pivotal roles in reshaping synaptic networks during neonatal brain development [41, 42]. They engulf synaptic elements by active synaptic pruning in an activity- and

complement-dependent manner [42]. Microglia-driven aberrant loss of synapses and consequent impairment of cognitive functions have also been reported in animal models of AD [35], infection [43], injury [44, 45], and aging [46]. Here we demonstrate that therapeutic doses of brain irradiation increase microglia phagocytic activity towards synaptic compartments and cause loss of dendritic spines with consequent impairments in memory functions.

Using RNA sequencing, we compared the transcriptomes of microglia from irradiated and non-irradiated brains after CSF-1Ri-mediated microglia depletion and repopulation. WBRT induces increased expression of genes that mainly belong to cell cycle regulation, DNA damage repair and stress-induced biological processes (Figure 1 d). As a result, activated microglia have higher engulfing potential towards both intrinsic and exotic synaptic compartments (Figures 6 and 7). This view is further supported by the increased expression of endosome/lysosome proteins CD68 and CD107a with the complement receptors CR3 and C5ar1 measured in microglia chronically after WBRT (Figure 7 e – g, and Supplementary Figure 2). Notably, both endosome/lysosome proteins and complement receptor expressions were comparable to naïve microglia (sham + control diet) in BEMs (WBRT + CSF-1Ri) and repopulated microglia (CSF-1Ri only). These results suggest that the loss of hippocampal synapses after WBRT may be dependent on the activation of the alternative complement pathway. Interestingly, although BEMs are morphologically similar to adult microglia, they retain a transcriptomic signature similar to both circulating monocytes and embryonic microglia (Figures 3 and 5). It is plausible that the BEMs are in a transitional state between peripheral monocytes and CNS microglia at early developmental stages.

Data from this study demonstrate that the changes in post-synaptic protein PSD95 level in hippocampal synaptosomes are in line with hippocampal dendritic spine counts (Figures 6 b and Feng et al[13]). However, pre-synaptic Synapsin 1 protein levels are not affected by WBRT or microglia depletion, suggesting that WBRT mainly induces loss of post-synaptic compartments.

Interestingly, although the phagocytosis potency of repopulated microglia and BEMs are both low (Figures 7 b and d), microglia depletion during WBRT results in higher dendritic spine densities compared to those with radiation alone, and microglia depletion alone (Figure 8 g, data re-plotted from Feng et al[13]). Finally, the protective effect of microglia depletion during WBRT in preserving memory functions extends to 3- and 6-months following irradiation (Figure 8 e and f). The dendritic spine density in mice that received WBRT and CS-1Ri remained higher than those who only received CSF-1Ri (Figure 8 h). These results indicate that, in an inactivated state (evidenced by no changes in genes involved in cell cycle and radiation response, in microglial phagocytosis and lysosome proteins, or in phagocytosis activity towards injected synaptosomes and latex beads) repopulated microglia and BEMs may have intrinsic differences in maintaining the homeostasis of dendritic spines (Figure 8 g), but these differences appears to diminish over time (Figure 8 h).

Further lineage tracing, transcriptomic and functional studies with different microglia depletion models will help answer the following questions: 1) whether the delayed engraftment of BEMs after WBRT seen at day 14 is due to the suppression of cell trafficking from the periphery to the CNS or survival of newly engrafted BEMs that depend on the CSF-1R. 2) The mechanism of the long-term maintenance of BEMs after WBRT. Whether it is achieved by continuous engraftment of new BEMs or by colonization of BEMs that are already in the brain parenchyma. 3) Long-term transcriptomic profile and function of BEMs, and their response to additional brain injuries.

In conclusion, we report for the first time the mechanism by which radiotherapy affect hippocampal synapses and memory functions. Our results demonstrate that replacement of CNS resident microglia by peripheral monocyte-derived BEMs results in a transcriptional and functional reset of immune cells in the brain to an inactive state, which protects against WBRT-induced dendritic spine loss in hippocampal neurons and recognition memory deficits. These

novel results suggest that repopulation of depleted microglia pool by peripheral monocytes derived BEMs represents a potent treatment for radiation-induced memory deficits.

Methods(up to 3000 words)

Animals: All experiments were conducted in compliance with protocols approved by the Institutional Animal Care and Use Committee at the University of California, San Francisco (UCSF), following the National Institutes of Health Guidelines for Animal Care. 7 weeks old C57BL/6J male mice were purchased from the Jackson Laboratory and housed at UCSF animal facilities and were provided with food and water ad libitum. All mice were habituated for one week before any treatments or procedures. 8–10 weeks old Cx3cr1$^{GFP/+}$Ccr2$^{RFP/+}$ mice were breed by crossing the Cx3cr1$^{GFP/GFP}$Ccr2$^{RFP/RFP}$ line with wildtype C57BL/6J mice, and used as donors for the bone marrow chimeras.

CSF-1Ri treatment: CSF-1Ri (PLX5622 formulated in AIN-76A standard chow at 1200 ppm, Research Diets, Inc) were provided by Plexxikon, Inc (Berkeley, CA). Mice were given free access to either CSF-1Ri chow or control diet (AIN-76A without PLX5622) for 21 days. Approximately 4.8 mg of PLX5622 was ingested by each mouse per day in the treated group (calculation based on 4 g/mouse daily consumption).

Fractionated whole-brain radiotherapy (WBRT): 8 weeks old mice were injected with ketamine (90mg/kg) /Xylazine (10 mg/kg) mix. When fully immobilized mice were placed in irradiator with cesium-137 source at the dose rate of 2.58 Gy/min. The body was shielded with a lead collimator that limited the radiation beam to a width of 1 cm to cover the brain. Three radiation fractions (3.3 Gy) were delivered every other day over 5 days. Sham animals received ketamine/xylazine without irradiation.

Bone marrow chimeras: 8 weeks old C57BL/6J mice were used as bone marrow recipients. 8 weeks old males received two doses of 6 Gy cersium-137 irradiation at the dose rate of 2.58 Gy/min with head protected by lead plates 6 hours apart. Bone marrow cells from 6–10 weeks old donors Cx3cr1$^{+/GFP}$Ccr2$^{+/RFP}$ or B6-EGFP (The Jackson Laboratory, stock No 003291) were isolated and resuspended in sterile saline at a concentration of 100 million cells/ml. 0.1 ml of

bone marrow cells were injected into recipients via retro-orbital injection immediately after the second head protected irradiation. Bone marrow chimeras were housed with 1.1 mg/ml neomycin as drinking water for 4 weeks and allowed an additional 2 weeks to recover before any treatments.

Synaptosome isolation staining and injection: Fresh hippocampi from a naïve mouse was homogenized and spun down in 0.32M sucrose solution (dissolved in 50 mM HEPES buffer). Supernatant was centrifuged in 0.65M sucrose solution at 12,000 rpm for 30 minutes at 4°C. The synaptosome containing pellet was resuspended in 1 x ice-cold PBS, diluted to 100 µg/ml, and stained with PSD-95 antibody (Millipore) on ice for 30 minutes followed by a secondary antibody staining (Invitrogen, goat anti-mouse AF488). Stained synaptosomes were washed and diluted 20 times in PBS and stored at -80°C. 2 µl of pre-stained synaptosomes were injected into the right hippocampus of each recipient mouse at the coordinate relative to the bregma: AP + 1.6 mm, ML + 1.6 mm and DV -2.0 mm. Mice were euthanized 3 days later. The left hemispheres (uninjected) were used for phagocytosis markers staining and the right hemispheres (injected) were used to assess synaptosome phagocytosis levels by flow cytometry or immunofluorescent staining.

Immunofluorescent Staining: hemi-brains with synaptosome injection were fixed in 4% PFA overnight, cryo-protected in 30% sucrose solution in 1 x PBS and sliced in 20 µm sections. Sliced tissues were stained with Iba1 (Fujifilm Wako Pure Chemical Corporation, 019-19741) followed by a secondary antibody staining (goat anti-rabbit AF568, Invitrogen, A-11011). DAPI was used for nuclear staining. Images close to the injection site (Supplementary Figure 1a) were taken using a Zeiss Imager Z1 microscope under a 20x objective lens. Tissues from bone marrow chimeras were processed and stained as described above. Images were taken using a CSU-W1 Nikon Spinning Disk Confocal microscope under 10x air, 20x air or 100x immerse oil

lenses. All images were analyzed using the Fiji/ImageJ software by experimenters blinded to sample information.

Behavior test: Novel Object Recognition (NOR) task was used to test hippocampal dependent recognition memory at one, three and six months after the last dose of irradiation. All tests took place during the dark cycle in a room with dim red light as previously described [13, 14]. Briefly, mice were habituated in an open arena (30 cm x 30 cm x 30 cm, L x W x H) for 10 minutes on day one and day two. On day three, two identical objects were put into the arena at a distance of 21 cm and mice were allowed to explore for 5 minutes. On day four, one object was replaced by a novel object and mice were allowed to explore for 5 minutes. All trials were recorded by an overhead camera and analyzed using Ethovision software. Data are presented as discrimination Index, calculated using fomular $DI = (T_{Novel} - T_{Familiar})/(T_{Novel} + T_{Familiar})$.

Flow cytometry: mice were perfused with cold PBS after euthanasia. Brains were immediately removed and dissociated using a Neural Tissue Dissociation kit (P) (Miltenyi Biotec). Brain cells were resuspended in 30% Percoll solution diluted in RPMI medium, and centrifuged at 800 g for 30 minutes at 4°C. Cell pellets were washed with FACS buffer (1 x DPBS with 0.5% BSA fraction V and 2% FBS), blocked with mouse CD16/32 Fc block (BD Biosciences #553141) and stained with fluorophore conjugated antibodies (CD11b-AF700, CD45-FITC, BD Pharmingen 557690 and 553080, C5aR-PE, CD68-PE and CD107a-PE, Miltenyi Biotec 130-106-174, 130-102-923 and 130-102-219), washed with FACS buffer and used for sort or analyses of bone marrow chimera efficiency. Data were collected on an Aria III sorter using the FACSDIVA software (BD Biosciences, V8.0.1), and analyzed with Flowjo software (FlowJo, LLC, V10.4.2).

Flow synaptometry: after isolation (described above) synaptosomes were stained with PSD-95 (Abcam ab13552) or Synapsin-1 (Millipore #1543) antibodies on ice for 30 minutes, washed and followed by a secondary antibody staining (Invitrogen, goat anti-mouse AF488, A-11001). Stained synaptosomes were used immediately for analysis of mean fluorescent intensity

measurement. Fluorescent latex beads of 1 µm, 2 µm, 3 µm and 6 µm were used as references of particle sizes in the FSC-A vs SSC-A dot plot. Events between 1 µm and 3 µm were used to measure mean fluorescent intensities of isolated synaptosomes under the FITC channel. Data were collected on an Aria III sorter using the FACSDIVA software, and analyzed with Flowjo software. At least 100,000 events were collected from each sample for the analyses.

RNA sequencing: mRNA was isolated from 100,000 to 400,000 sorted microglia or BEMs using the Dynabeads mRNA DIRECT Purification Kit (Invitrogen #61011) following the manufacturer's instructions. RNA sequencing libraries were generated using the Ovation RNA-seq system V2 and Ultralow Library Construction System sample prep kits (NuGEN). Libraries were sequenced on the HiSeq 2500 to generate single end 50bp reads according to the manufacturer's instructions. Normalized per-gene read counts were used to compare relative gene expression levels across samples. Only genes with average read counts greater than 10 were included for analyses. Heatmaps were drawn using the online analysis software Morpheus (Broad Institute, https://software.broadinstitute.org/morpheus), followed by hierarchical clustering using the One minus pearson correlation method. Gene Ontology analysis was performed using the Statistical overrepresentation test (GO biological process complete, PANTHER version 14) [47]. Bar graphs to visualize fold enrichment and p values of enriched GO biological pathways were drawn using the GraphPad Prism software (V 7.01, GraphPad Software, Inc). For analysis of monocyte/microglia signature genes, dataset from Lavin and Winter et al was used as reference (GSE63340) [30]. Genes significantly up or down regulated ($p<0.05$, fold-change > 1.5 or <0.667) in monocytes vs microglia comparisons are defined as monocyte or microglia signature genes, respectively. Heatmaps were drawn as described above, and similarity matrix were drawn using the Morpheus online tool with Pearson correlation. Monocyte/microglia similarity scores were calculated based on the numbers of genes in each treatment group from this study that expressed in the same trend as monocyte/microglia

signature genes (genes with fold-change between 0.6667 and 1.500 or with p>0.05 were defined as unspecified). For juvenile/embryonic signature analysis, dataset from Matcovitch-Natan and Winter et al was used as reference (GSE79819) [32]. Gene listed to be highly expressed in Yolk Sac and embryonic day 10.5–12.5 were defined as embryonic/juvenile microglia signatures, genes highly expressed in adult cortex/hippocampus/spinal cord were defined as adult microglia signatures. Heatmaps, similarity matrix and similarity scores were drawn or calculated as described above.

qPCR: mRNAs were extracted from sorted microglia using the Dynabeads mRNA DIRECT Purification Kit (Invitrogen #61011), and reverse transcribed into cDNAs using reverse transcription kit (info) . qPCR reactions were set up in duplicate reactions using the PowerUp SYBR Green Master Mix kit (Applied Biosystems #A25777) using an Mx3000P qPCR System (Agilent, Santa Clara, CA) following the manufacturer's instructions. Data were analyzed using the standard curve method. Standard cDNAs were generated with total RNAs from mixed naïve and irradiated mouse brains. qPCR primers sequences are listed in Supplementary Table 4.

Statistical analyses: Two-way ANOVA was used to determine radiation and CSF-1Ri treatment effects for NOR, qPCR, flowsynaptometry, flow cytometry, immunofluorescent staining counts and dendritic spine count results, with Tukey's post hoc multiple comparisons (Figures 1a, 2 a–h, 4 a–h, 6b, 7b, d–g). One-way ANOVA with Sidak's post hoc multiple comparisons was used to determine effect of developmental stages for dataset published by Matcovitch-Natan and Winter et al (Figure 5a). Unpaired t-test was used to determine differentially expressed microglia/monocyte signature genes from dataset published by Lavin and Winter et al (Figure 3d). Unpaired t-test was used calculate the p value of the comparison of BEMs contributions between the BMT and BMT + WBRT groups (Figure 3c). Exact p values and numbers of animals used in each experiment were listed in each related figure legend. All error bars represent mean ± SEM.

Figure Legends

Figure 1: CSF-1R inhibitor-mediated depletion resets radiation-induced transcriptomic changes in microglia. **a** experimental design and Novel Object Recognition (NOR) test result. CSF-1R inhibitor was used to deplete microglia during 3 doses of 3.3 Gy of whole-brain radiotherapy (WBRT). A 4-day NOR protocol was used to measure recognition memory, which ended on day 32 post WBRT. Microglia were isolated using fluorescent activated cell sorting (FACS) on day 33. **b** dot plots showing NOR results. Statistical analysis was performed using two-way ANOVA with Dunnett's multiple comparisons test. There is no CSF-1Ri treatment effect ($F(1,38)=1.787$, $p=0.1893$), but significant WBRT effect ($F(1, 38)=13.23$, $p=0.0008$) and interaction between CSF-1Ri treatment and WBRT ($F(1,38)=6.07$, $p=0.0184$), N = 9-12, animals with insufficient exploration time on NOR test day were excluded. Hollow squares represent animals used in RNA sequencing. **c** hierarchically clustered heatmap showing significantly altered microglial genes by WBRT, but not changed with CSF-1Ri treatment. **d** bar graphs summarizing fold enrichment and p values of the top 20 enriched Biological Processes by Gene Ontology analysis from up-regulated microglial genes after WBRT (full list in Supplementary Table1). No significantly enriched terms were identified by GO analysis from down-regulated genes by WBRT. **e** a pie chart summarizing all enriched GOBP terms. ns= not significant, ***$p<0.0001$.

Figure 2: qPCR validation of radiation-induced genes. Genes from highly enriched GOBP terms were selected to validate RNAseq results. **a** and **b** Toll-like receptor 3 signaling pathway: *Lgals9* and *TNFα*. **c-e** Cellular response to ionizing radiation: *Rad51*, *Mdm2* and *Ddias*. **d** and **f** Regulation of response to reactive oxygen species: *TNFα* and *Sesn2*. **c, g and h** Regulation of double-strand break repair: *Rad51*, *Foxm1* and *Chek1*. Statistical analyses were performed using two-way ANOVA with Tukey's multiple comparisons test. *$p<0.05$, **$p<0.01$, ***$p<0.001$,

****p<0.0001. N = 4–6. The qPCR experiments were performed in duplicates with similar results. Figures shown here are representative results from one experiment.

Figure 3: Repopulated microglia-like cells after depletion and WBRT originate from peripheral monocytes and retain monocytic signatures. **a** experimental design of head-protected bone marrow transplantation (BMT) followed by CSF-1Ri-mediated microglia depletion and WBRT. Lower panel shows fur colors before euthanasian for brain analysis. **b** representative FACS analysis gating strategy to analyze bone marrow chimera efficiency 6 weeks after BMT, about two thirds of the $CD11b^{+}Ly6C^{high}$ monocytes are replaced by $GFP^{+}RFP^{+}$ cells derived from donor bone marrow cells. **c** representative FACS analysis gating strategy and brain myeloid composition results. Upper panel shows FACS gating using CD45 and CD11b staining; microglia and microglia-like cells are defined by positive CD11b staining and low or intermediate CD45 levels. Lower panel shows scatter plots of GFP/RFP fluorescent levels of the $CD11b^{+}CD45^{low/intermediate}$ population in the brain, and a dot plot comparing percentages of peripheral myeloid cell derived microglia-like cells. Statistical analysis was performed using unpaired t-test, ***p<0.001. **d** hierarchically clustered heatmaps to compare microglia and monocyte signatures. A signature gene list was defined using a dataset published by Lavin and Winter et al, GSE63340. Defined list and expression details are in Supplementary Table 2). **e** Similarity matrix comparisons using defined monocyte and microglia signature genes. **f** bar graph showing similarity scores to compare relative numbers of genes (in percentage of the defined list) that express in the same trends as monocytes or microglia based on the Lavin and Winter *et al* dataset.

Figure 4: qPCR validation of microglia- and monocyte-specific genes. Selected genes that are known to highly express in microglia or monocytes were used to validate RNAseq results. **a – d** microglia signature genes *Sall1*, *P2ry12*, *Tmem119* and *Trem2* have lower expression levels in monocyte derived BEMs (CSF-1Ri + WBRT) compared to naïve microglia (control diet sham), irradiated microglia (control diet + WBRT) and repopulated microglia (CSF-1Ri sham). **e – f** monocyte signature genes *Runx3*, *Lpar6* and *Pmepa1* have higher expression levels in BEMs compared to other groups. Statistical analyses were performed using two-way ANOVA with Tukey's multiple comparisons test. *$p<0.05$, **$p<0.01$, ***$p<0.001$, ****$p<0.0001$. N = 4 – 6. The qPCR experiments were performed in duplicates with similar results. Figures shown here are representative results from one experiment.

Figure 5: Monocyte-derived BEMs after WBRT have embryonic microglia signatures. **a** hierarchically clustered heatmaps to compare embryonic and adult microglia signatures across samples. Embryonic and adult signature genes were defined based on published dataset by Matchonitch and Winter et al. (Gene list and expression data in Supplementary Table 3). **b** Similarity matrix comparisons using defined embryonic and adult signature genes. **c** bar graph showing similarity scores to compare relative numbers of genes (shown as percentage of the defined list) that express in the same trends as embryonic or adult microglia in the Matchovitch and Winter dataset.

Figure 6: Microglia depletion during WBRT prevents WBRT-induced decrease of PSD-95 in synaptosomes. **a** scatter plots showing gating strategy in flowsynaptometry analyses. Fluorescent beads at various sizes were used as standard to gate isolated hippocampal cell membrane fractions. Particles between 1 µm and 3 µm were considered synaptosomes and

used to determine PSD95 and Synapsin1 protein levels by mean fluorescent intensities (MFIs). **b** dot plots to compare PSD95 and Synapsin 1 MFI levels in hippocampal cell fractions. Statistical analyses were performed using two-way ANOVA with Tukey's multiple comparisons test. ns = not significant, *p<0.05, ***p<0.001. N=6.

Figure 7: Repopulated microglia and brain-engrafted macrophages are not activated and phagocyte less synaptic compartments. **a** experimental design for in vivo synaptosome phagocytosis assays. Injection of pre-stained synaptosomes was timed to be the same as previous experiments. Three days later, on day 36 after WBRT, ipsilateral hemispheres were harvested and used for engulfment measurement using FACS or Immunofluorescent staining. **b** FACS analysis result showing percentage of microglia that were positive of pre-stained PSD-95 signals. **c** representative images showing engulfment of pre-stained synaptosomes by microglia near injection site. White arrows point at microglia that have engulfed pre-stained synaptosomes. scale bar = 20 µm. **d** dot plot to show quantification result of synaptosome engulfment by immunofluorescent staining. **e – g** dot plots showing cell surface C5aR, and intracellular CD68 and CD107a protein levels in microglia and BEMs. Statistical analyses were performed using two-way ANOVA with Tukey's multiple comparisons test. *p<0.05, **p<0.01, ***p<0.001, ****p<0.0001. N = 5 – 6.

Figure 8: Replacement of microglia by brain-engrafted macrophages provides long-term protection against WBRT-induced recognition memory deficits and dendritic spine loss. **a,** schematic of experimental design for long-term assessment of BEMs. **b** representative images of microglia/BEMs counting, scale bar = 20 µm. **c** dot plot to show percentage of replacement of microglia by BEMs, each dot represent an individual mouse. **d** schematic of experimental

design for long-term memory and dendritic spine density analyses. **e** and **f** dot plots to show NOR test results at 3 and 6 months after WBRT, respectively. N = 6–12. **g** dendritic spine counts of hippocampal granule neurons at 1 month after WBRT (figure reproduced using our previously published data Feng et al[48]). **h** dendritic spine counts of hippocampal granule neurons at 6 months after WBRT, N = 5 – 6.. Statistical analyses were performed using unpaired t-test for each time point (**c**) or two-way ANOVA with Tukey's multiple comparisons test (**e** - **h**). *p<0.05, **p<0.01, ***p<0.001, ****p<0.0001.

Acknowledgements (optional)

This work was funded by grants from the National Institutes of Health no. R01CA133216 and R01CA213441 (S.R.).

Author contributions

X.F. conceptualized the study, designed and performed the experiments, analyzed the data and wrote the manuscript. D.C. assisted in the in vivo phagocytosis assay and data analysis. S.G analyzed the long-term dendritic spine counts data. S.L. provided assistance in experiments related to WBRT and BM chimeras. N.G. provided critical inputs to the study and revised the manuscript. S.R. conceptualized and supervised the study and revised the manuscript. All authors approved the final version of the manuscript.

Competing interests

The authors declare no competing interests.

Reference

1. Alliot, F., Godin, I. & Pessac, B. Microglia derive from progenitors, originating from the yolk sac, and which proliferate in the brain. *Developmental Brain Research* **117**, 145-152 (1999).
2. Ginhoux, F. *et al.* Fate Mapping Analysis Reveals That Adult Microglia Derive from Primitive Macrophages. *Science* **330**, 841 (2010).
3. Ajami, B., Bennett, J.L., Krieger, C., Tetzlaff, W. & Rossi, F.M.V. Local self-renewal can sustain CNS microglia maintenance and function throughout adult life. *Nature Neuroscience* **10**, 1538 (2007).
4. Prinz, M., Priller, J., Sisodia, S.S. & Ransohoff, R.M. Heterogeneity of CNS myeloid cells and their roles in neurodegeneration. *Nat Neurosci* **14**, 1227-1235 (2011).
5. Saijo, K. & Glass, C.K. Microglial cell origin and phenotypes in health and disease. *Nat Rev Immunol* **11**, 775-787 (2011).
6. Hong, S., Dissing-Olesen, L. & Stevens, B. New insights on the role of microglia in synaptic pruning in health and disease. *Current opinion in neurobiology* **36**, 128-134 (2015).
7. Hong, S. & Stevens, B. Microglia: Phagocytosing to Clear, Sculpt, and Eliminate. *Developmental Cell* **38**, 126-128 (2016).
8. Elmore, M.R. *et al.* Colony-stimulating factor 1 receptor signaling is necessary for microglia viability, unmasking a microglia progenitor cell in the adult brain. *Neuron* **82**, 380-397 (2014).
9. Elmore, M.R., Lee, R.J., West, B.L. & Green, K.N. Characterizing newly repopulated microglia in the adult mouse: impacts on animal behavior, cell morphology, and neuroinflammation. *PLoS One* **10**, e0122912 (2015).
10. Dagher, N.N. *et al.* Colony-stimulating factor 1 receptor inhibition prevents microglial plaque association and improves cognition in 3xTg-AD mice. *Journal of neuroinflammation* **12**, 139 (2015).
11. Spangenberg, E.E. *et al.* Eliminating microglia in Alzheimer's mice prevents neuronal loss without modulating amyloid-β pathology. *Brain* (2016).
12. Acharya, M.M. *et al.* Elimination of microglia improves cognitive function following cranial irradiation. *Scientific reports* **6**, 31545 (2016).
13. Feng, X. *et al.* Colony-stimulating factor 1 receptor blockade prevents fractionated whole-brain irradiation-induced memory deficits. *Journal of neuroinflammation* **13**, 215 (2016).

14. Feng, X., Liu, S., Chen, D., Rosi, S. & Gupta, N. Rescue of cognitive function following fractionated brain irradiation in a novel preclinical glioma model. *eLife* **7**, e38865 (2018).
15. Krukowski, K. *et al.* Temporary microglia-depletion after cosmic radiation modifies phagocytic activity and prevents cognitive deficits. *Scientific reports* **8**, 7857 (2018).
16. Rapp, S.R. *et al.* Donepezil for Irradiated Brain Tumor Survivors: A Phase III Randomized Placebo-Controlled Clinical Trial. *Journal of Clinical Oncology* **33**, 1653-1659 (2015).
17. Stupp, R. *et al.* Radiotherapy plus Concomitant and Adjuvant Temozolomide for Glioblastoma. *New England Journal of Medicine* **352**, 987-996 (2005).
18. Greene-Schloesser, D. & Robbins, M.E. Radiation-induced cognitive impairment--from bench to bedside. *Neuro Oncol* **14 Suppl 4**, iv37-44 (2012).
19. Shinohara, C., Gobbel, G.T., Lamborn, K.R., Tada, E. & Fike, J.R. Apoptosis in the Subependyma of Young Adult Rats after Single and Fractionated Doses of X-Rays. *Cancer Research* **57**, 2694-2702 (1997).
20. Morganti, J.M., Jopson, T.D., Liu, S., Gupta, N. & Rosi, S. Cranial Irradiation Alters the Brain's Microenvironment and Permits $CCR2^{+}$ Macrophage Infiltration. *PLoS ONE* **9**, e93650 (2014).
21. Warrington, J.P. *et al.* Whole Brain Radiation-Induced Vascular Cognitive Impairment: Mechanisms and Implications. *Journal of Vascular Research* **50**, 445-457 (2013).
22. Hua, K., Schindler, M.K., McQuail, J.A., Forbes, M.E. & Riddle, D.R. Regionally distinct responses of microglia and glial progenitor cells to whole brain irradiation in adult and aging rats. *PLoS One* **7**, e52728 (2012).
23. Chiang, C.S., McBride, W.H. & Withers, H.R. Radiation-induced astrocytic and microglial responses in mouse brain. *Radiotherapy and Oncology* **29**, 60-68 (1993).
24. Mizumatsu, S. *et al.* Extreme Sensitivity of Adult Neurogenesis to Low Doses of X-Irradiation. *Cancer Research* **63**, 4021-4027 (2003).
25. Monje, M.L. *et al.* Impaired human hippocampal neurogenesis after treatment for central nervous system malignancies. *Annals of Neurology* **62**, 515-520 (2007).
26. Mildner, A. *et al.* Microglia in the adult brain arise from Ly-6ChiCCR2+ monocytes only under defined host conditions. *Nat Neurosci* **10**, 1544-1553 (2007).
27. Priller, J. *et al.* Targeting gene-modified hematopoietic cells to the central nervous system: Use of green fluorescent protein uncovers microglial engraftment. *Nature Medicine* **7**, 1356-1361 (2001).
28. Jung, S. *et al.* Analysis of Fractalkine Receptor CX₃CR1 Function by Targeted Deletion and Green Fluorescent Protein Reporter Gene Insertion. *Molecular and cellular biology* **20**, 4106 (2000).
29. Saederup, N. *et al.* Selective Chemokine Receptor Usage by Central Nervous System Myeloid Cells in CCR2-Red Fluorescent Protein Knock-In Mice. *PLoS ONE* **5**, e13693 (2010).
30. Lavin, Y. *et al.* Tissue-resident macrophage enhancer landscapes are shaped by the local microenvironment. *Cell* **159**, 1312-1326 (2014).
31. Cronk, J.C. *et al.* Peripherally derived macrophages can engraft the brain independent of irradiation and maintain an identity distinct from microglia. *The Journal of experimental medicine* **215**, 1627-1647 (2018).
32. Matcovitch-Natan, O. *et al.* Microglia development follows a stepwise program to regulate brain homeostasis. *Science* **353**, aad8670 (2016).
33. Fein, J.A. *et al.* Co-localization of amyloid beta and tau pathology in Alzheimer's disease synaptosomes. *The American journal of pathology* **172**, 1683-1692 (2008).
34. Prieto, G.A. *et al.* Synapse-specific IL-1 receptor subunit reconfiguration augments vulnerability to IL-1β in the aged hippocampus. *Proceedings of the National Academy of Sciences* **112**, E5078 (2015).

35. Hong, S. *et al.* Complement and microglia mediate early synapse loss in Alzheimer mouse models. *Science* (2016).
36. Stevens, B. *et al.* The classical complement cascade mediates CNS synapse elimination. *Cell* **131**, 1164-1178 (2007).
37. Tay, T.L. *et al.* A new fate mapping system reveals context-dependent random or clonal expansion of microglia. *Nature Neuroscience* **20**, 793 (2017).
38. Huang, Y. *et al.* Repopulated microglia are solely derived from the proliferation of residual microglia after acute depletion. *Nat Neurosci* **21**, 530-540 (2018).
39. Ajami, B., Bennett, J.L., Krieger, C., McNagny, K.M. & Rossi, F.M.V. Infiltrating monocytes trigger EAE progression, but do not contribute to the resident microglia pool. *Nat Neurosci* **14**, 1142-1149 (2011).
40. Yamasaki, R. *et al.* Differential roles of microglia and monocytes in the inflamed central nervous system. *The Journal of experimental medicine* **211**, 1533-1549 (2014).
41. Vainchtein, I.D. *et al.* Astrocyte-derived interleukin-33 promotes microglial synapse engulfment and neural circuit development. *Science* **359**, 1269 (2018).
42. Schafer, Dorothy P. *et al.* Microglia Sculpt Postnatal Neural Circuits in an Activity and Complement-Dependent Manner. *Neuron* **74**, 691-705 (2012).
43. Vasek, M.J. *et al.* A complement-microglial axis drives synapse loss during virus-induced memory impairment. *Nature* **534**, 538-543 (2016).
44. Norris, G.T. *et al.* Neuronal integrity and complement control synaptic material clearance by microglia after CNS injury. *The Journal of experimental medicine* (2018).
45. Krukowski, K. *et al.* Traumatic Brain Injury in Aged Mice Induces Chronic Microglia Activation, Synapse Loss, and Complement-Dependent Memory Deficits. *International Journal of Molecular Sciences* **19** (2018).
46. Shi, Q. *et al.* Complement C3-Deficient Mice Fail to Display Age-Related Hippocampal Decline. *The Journal of neuroscience : the official journal of the Society for Neuroscience* **35**, 13029-13042 (2015).
47. Mi, H., Muruganujan, A., Ebert, D., Huang, X. & Thomas, P.D. PANTHER version 14: more genomes, a new PANTHER GO-slim and improvements in enrichment analysis tools. *Nucleic acids research* **47**, D419-D426 (2019).
48. Feng, X. *et al.* Loss of CX3CR1 increases accumulation of inflammatory monocytes and promotes gliomagenesis. *Oncotarget; Vol 6, No 17* (2015).

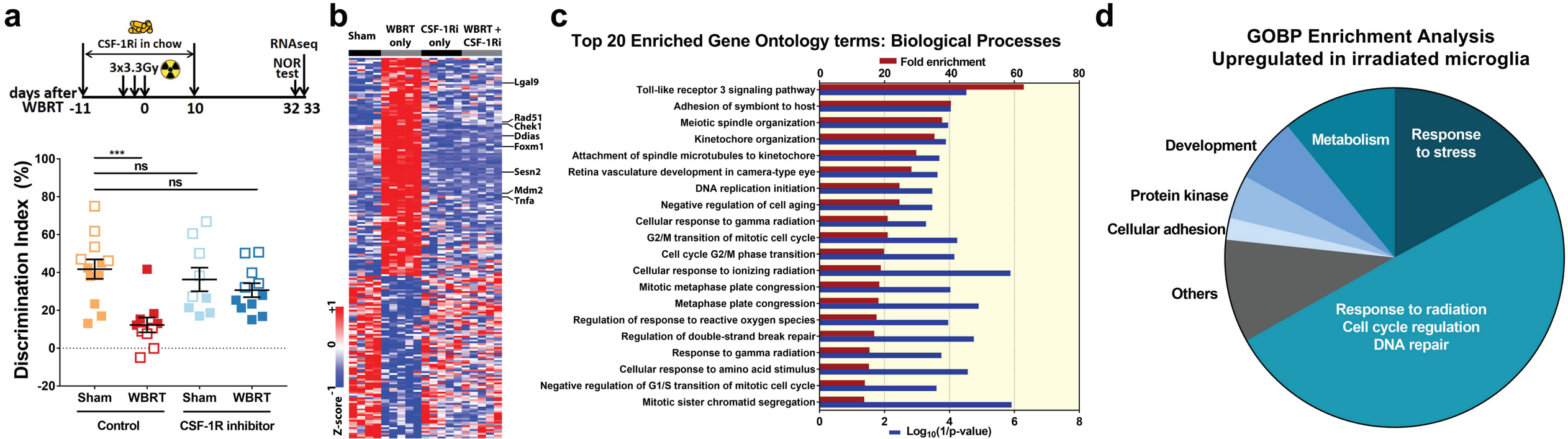
a
CSF-1Ri in chow
3x3.3Gy
RNAseq
NOR test
days after WBRT -11
0
10
32 33
Discrimination Index (%)
***
ns
ns
Sham
WBRT
Sham
WBRT
Control
CSF-1R inhibitor
b
Sham
WBRT only
CSF-1Ri only
WBRT + CSF-1Ri
Lgal9
Rad51
Chek1
Ddias
Foxm1
Sesn2
Mdm2
Tnfa
Z-score
c
Top 20 Enriched Gene Ontology terms: Biological Processes
Fold enrichment
Toll-like receptor 3 signaling pathway
Adhesion of symbiont to host
Meiotic spindle organization
Kinetochore organization
Attachment of spindle microtubules to kinetochore
Retina vasculature development in camera-type eye
DNA replication initiation
Negative regulation of cell aging
Cellular response to gamma radiation
G2/M transition of mitotic cell cycle
Cell cycle G2/M phase transition
Cellular response to ionizing radiation
Mitotic metaphase plate congression
Metaphase plate congression
Regulation of response to reactive oxygen species
Regulation of double-strand break repair
Response to gamma radiation
Cellular response to amino acid stimulus
Negative regulation of G1/S transition of mitotic cell cycle
Mitotic sister chromatid segregation
Log10(1/p-value)
d
GOBP Enrichment Analysis
Upregulated in irradiated microglia
Development
Metabolism
Response to stress
Protein kinase
Cellular adhesion
Others
Response to radiation
Cell cycle regulation
DNA repair

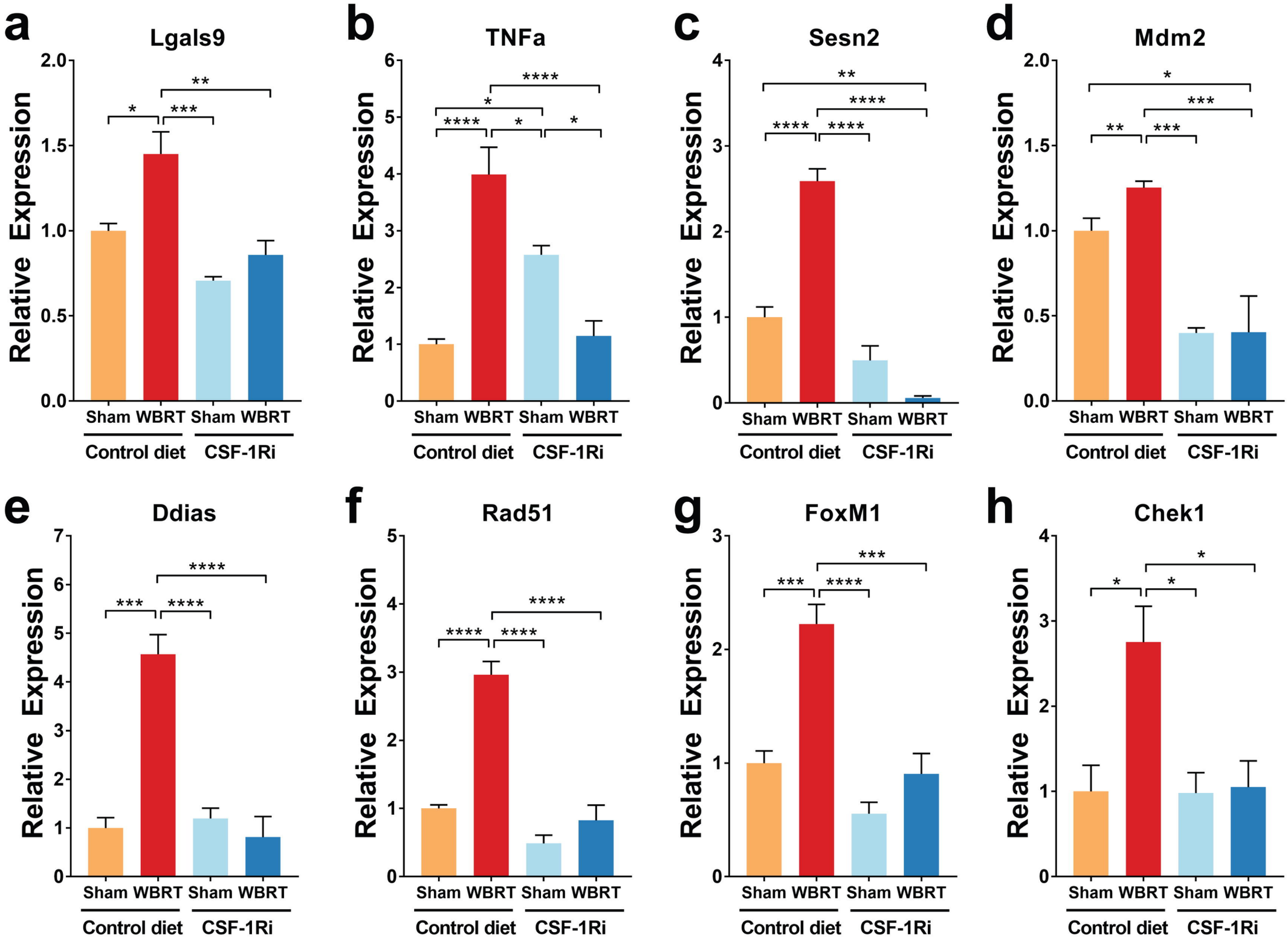
a
Lgals9
Relative Expression
2.0
1.5
1.0
0.5
0.0
*
***
**
Sham WBRT Sham WBRT
Control diet CSF-1Ri
b
TNFa
Relative Expression
6
5
4
3
2
1
0
****
*
****
*
*
Sham WBRT Sham WBRT
Control diet CSF-1Ri
c
Sesn2
Relative Expression
4
3
2
1
0
**
****
****
****
Sham WBRT Sham WBRT
Control diet CSF-1Ri
d
Mdm2
Relative Expression
2.0
1.5
1.0
0.5
0.0
*
***
**
***
Sham WBRT Sham WBRT
Control diet CSF-1Ri
e
Ddias
Relative Expression
7
6
5
4
3
2
1
0
****
***
****
Sham WBRT Sham WBRT
Control diet CSF-1Ri
f
Rad51
Relative Expression
5
4
3
2
1
0
****
****
****
Sham WBRT Sham WBRT
Control diet CSF-1Ri
g
FoxM1
Relative Expression
3
2
1
0
***
***
****
Sham WBRT Sham WBRT
Control diet CSF-1Ri
h
Chek1
Relative Expression
4
3
2
1
0
*
*
*
Sham WBRT Sham WBRT
Control diet CSF-1Ri

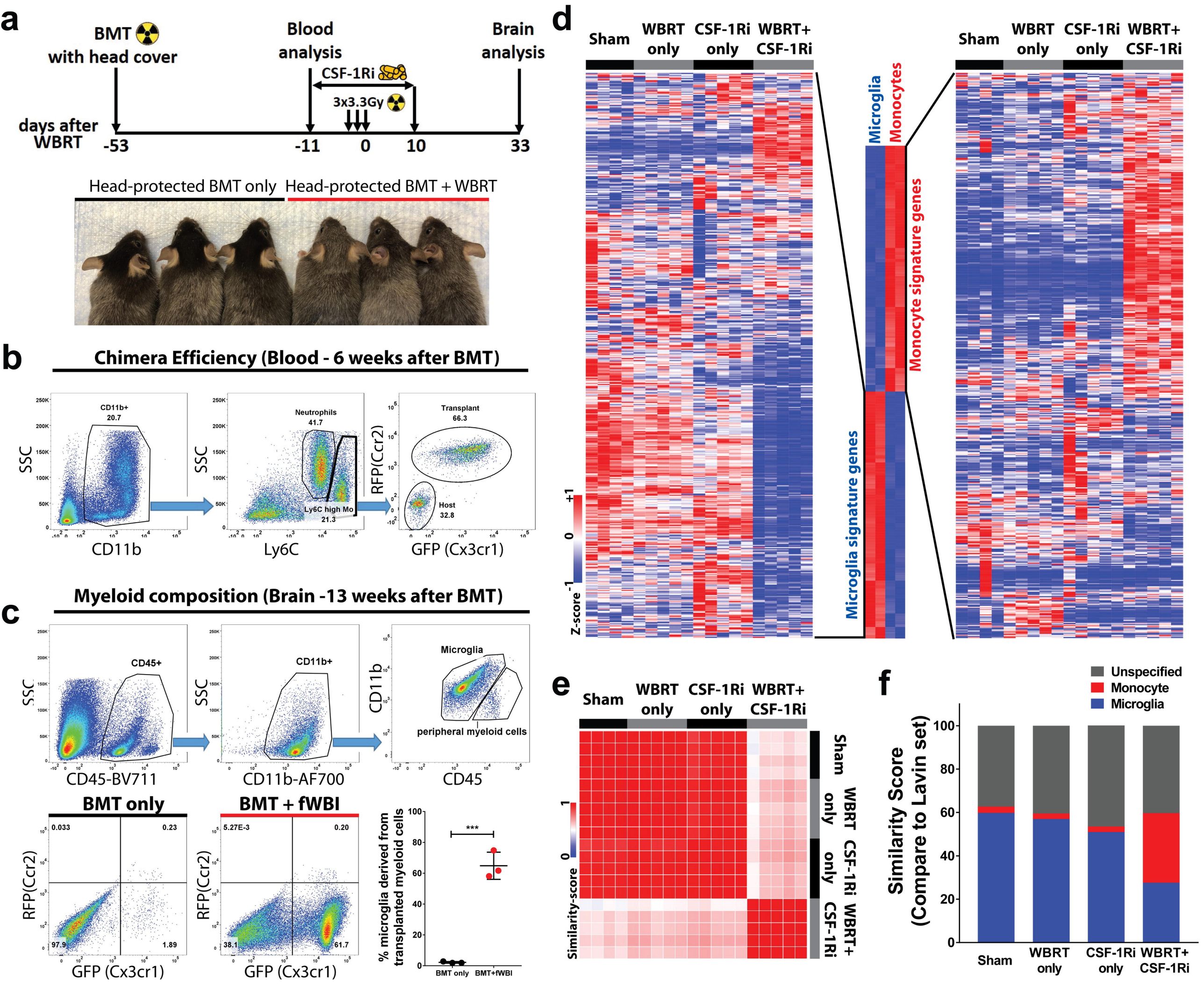
a
BMT with head cover
Blood analysis
Brain analysis
CSF-1Ri
3x3.3Gy
days after WBRT
-53
-11
0
10
33
Head-protected BMT only
Head-protected BMT + WBRT
b
Chimera Efficiency (Blood - 6 weeks after BMT)
CD11b+ 20.7
Neutrophils 41.7
Ly6C high Mo 21.3
Transplant 66.3
Host 32.8
SSC
CD11b
Ly6C
RFP(Ccr2)
GFP (Cx3cr1)
c
Myeloid composition (Brain -13 weeks after BMT)
CD45+
CD11b+
Microglia
peripheral myeloid cells
CD45-BV711
CD11b-AF700
CD45
BMT only
BMT + fWBI
0.033
0.23
97.9
1.89
5.27E-3
0.20
38.1
61.7
% microglia derived from transplanted myeloid cells
***
BMT only
BMT+fWBI
d
Sham
WBRT only
CSF-1Ri only
WBRT+ CSF-1Ri
Microglia
Monocytes
Monocyte signature genes
Microglia signature genes
Z-score
+1
0
-1
e
Similarity-score
f
Unspecified
Monocyte
Microglia
Similarity Score (Compare to Lavin set)

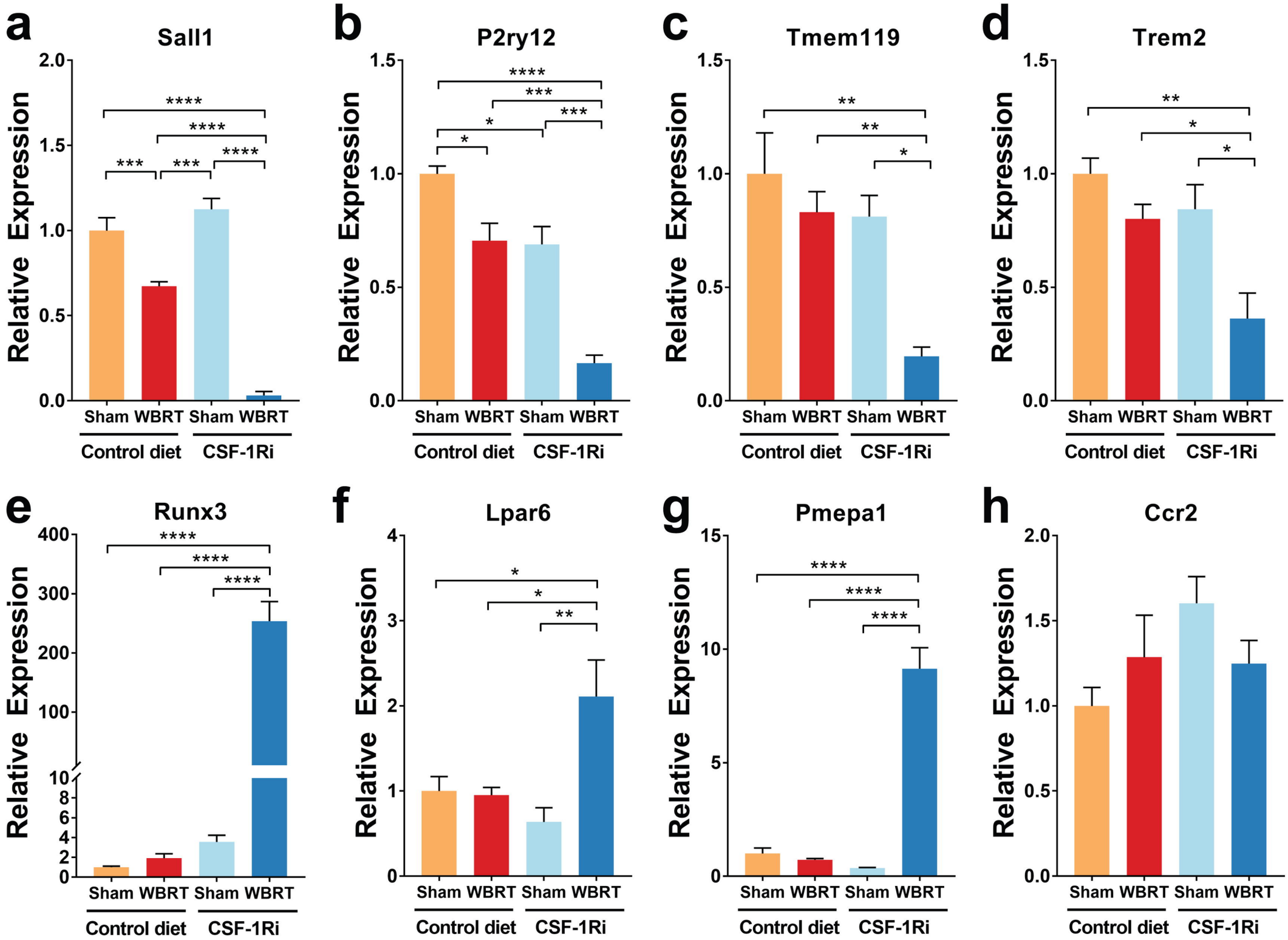
a
Sall1
b
P2ry12
c
Tmem119
d
Trem2
e
Runx3
f
Lpar6
g
Pmepa1
h
Ccr2
Relative Expression
Sham WBRT Sham WBRT
Control diet CSF-1Ri

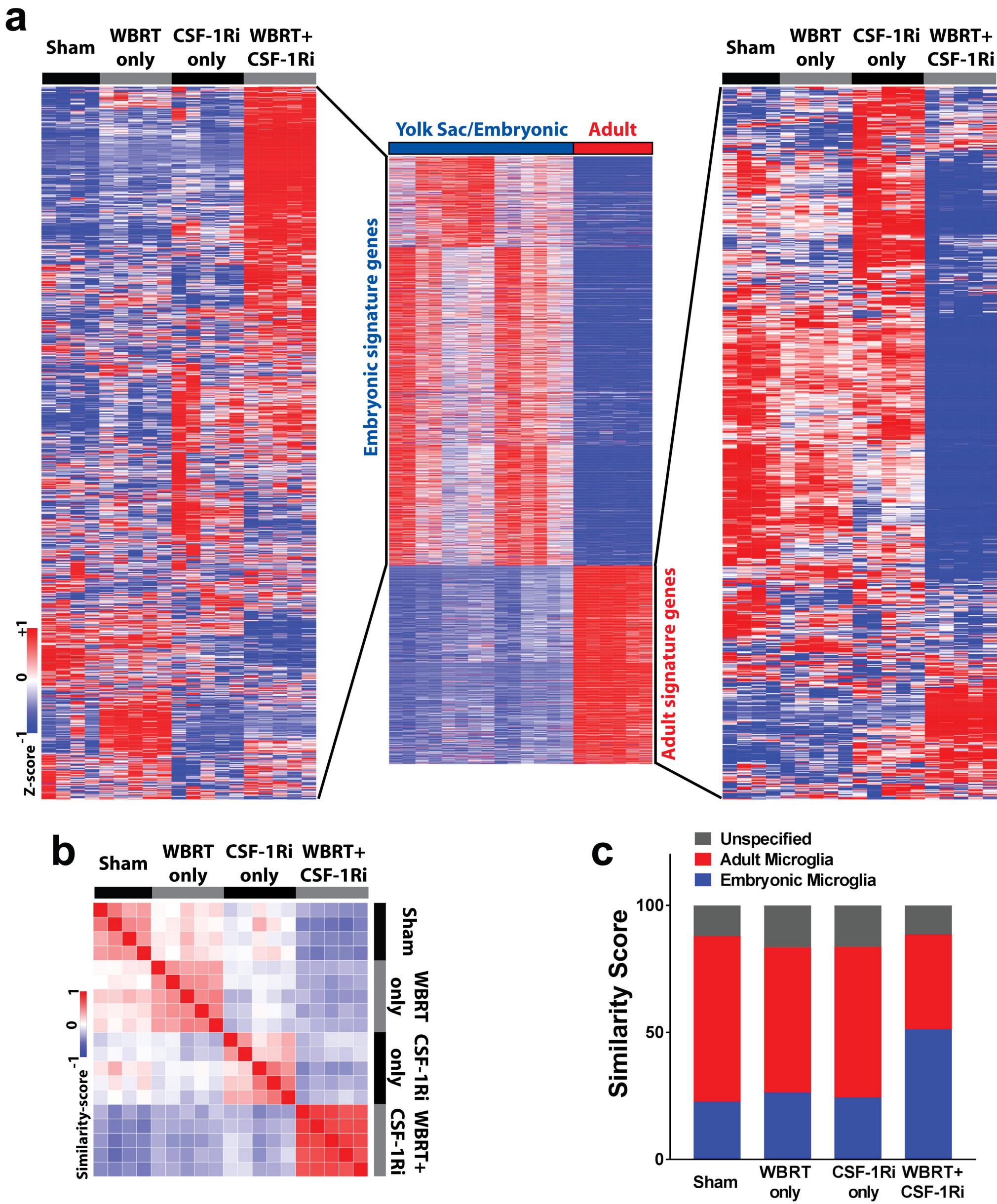
a
Sham
WBRT only
CSF-1Ri only
WBRT+ CSF-1Ri
Z-score
+1
0
-1
Yolk Sac/Embryonic
Adult
Embryonic signature genes
Adult signature genes
b
Similarity-score
c
Unspecified
Adult Microglia
Embryonic Microglia
Similarity Score
100
50
0

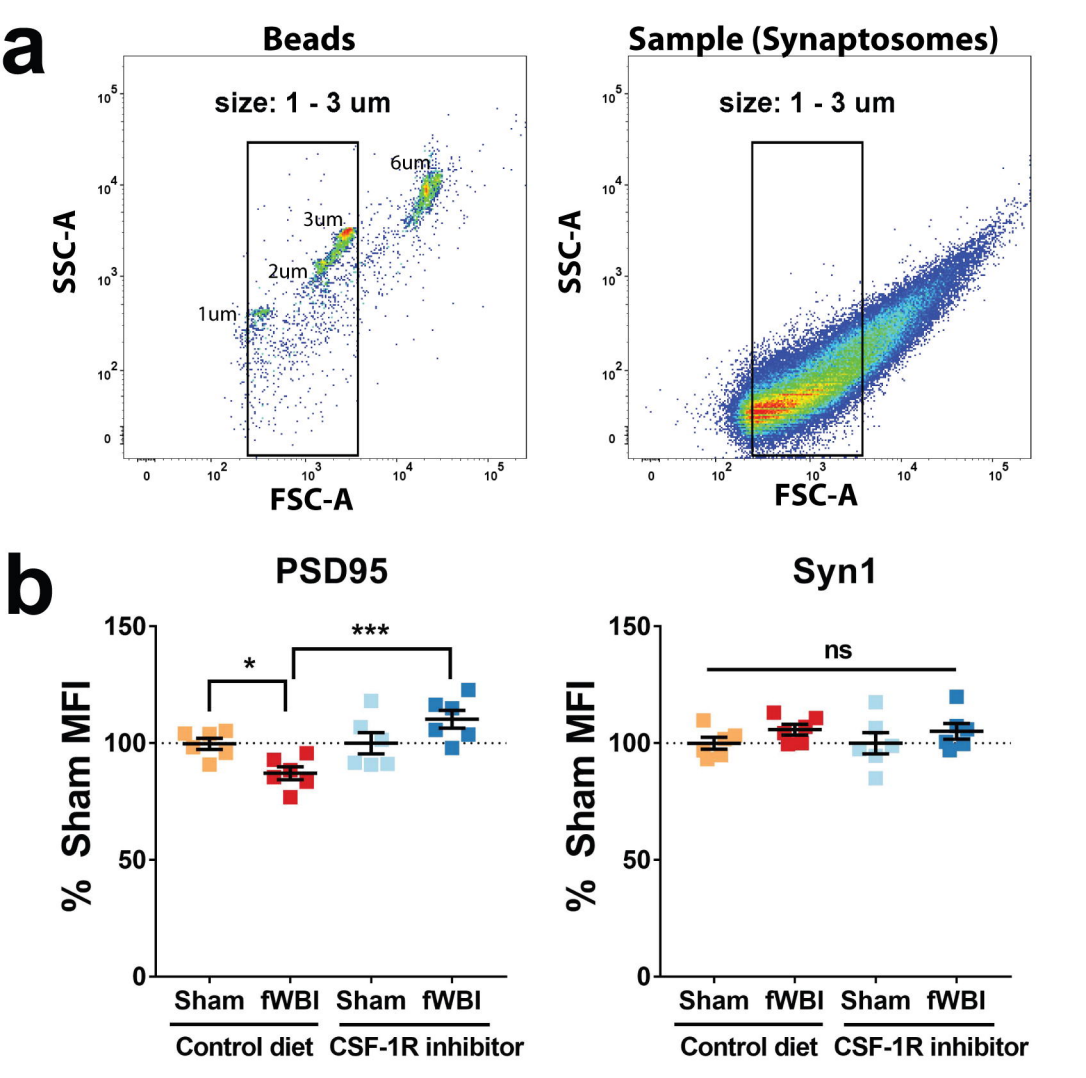
a
Beads
size: 1 - 3 um
6um
3um
2um
1um
SSC-A
FSC-A
Sample (Synaptosomes)
size: 1 - 3 um
SSC-A
FSC-A
b
PSD95
% Sham MFI
150
100
50
0
*
***
Sham
fWBI
Sham
fWBI
Control diet
CSF-1R inhibitor
Syn1
% Sham MFI
150
100
50
0
ns
Sham
fWBI
Sham
fWBI
Control diet
CSF-1R inhibitor

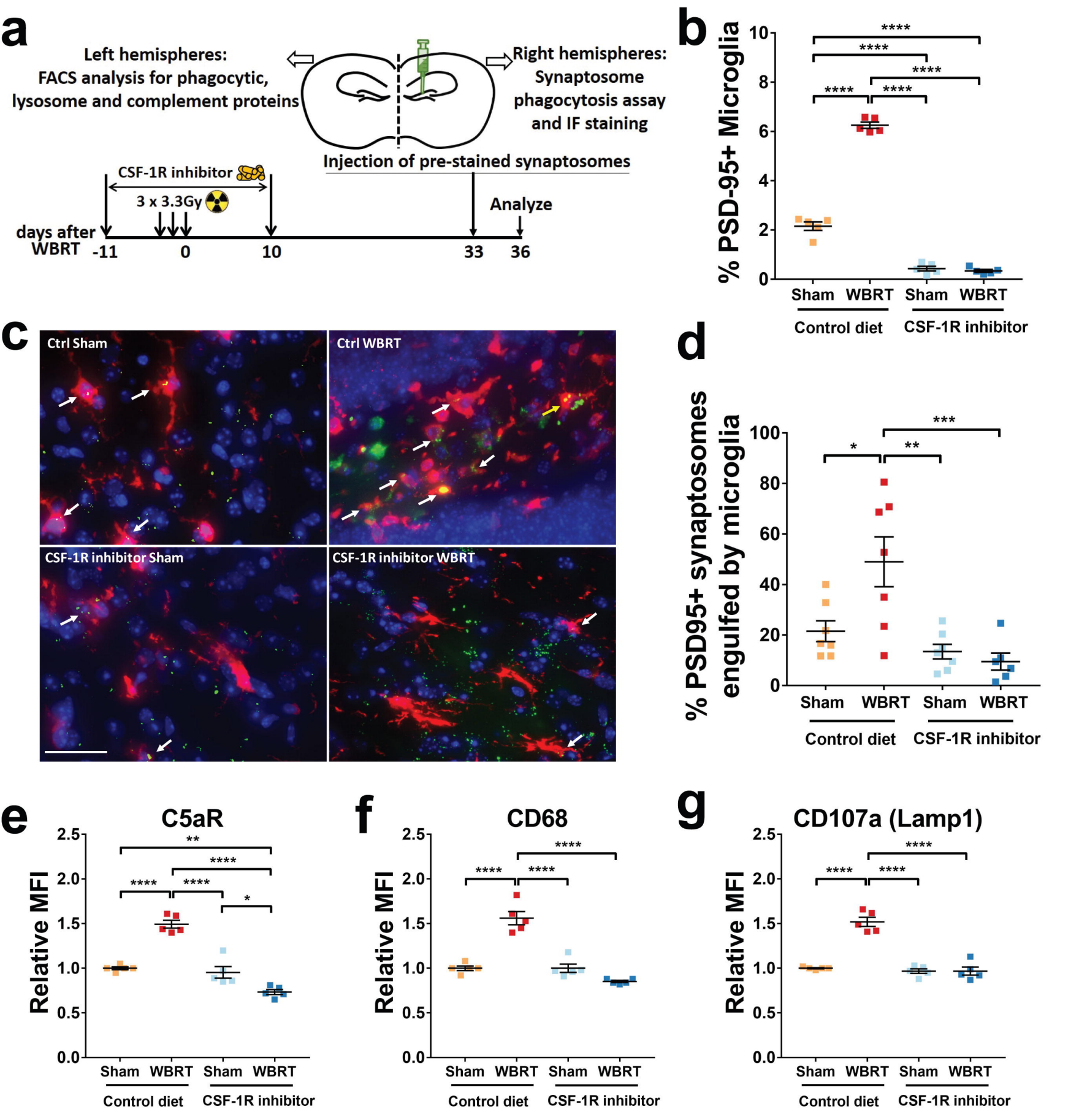
a
Left hemispheres:
FACS analysis for phagocytic, lysosome and complement proteins
Right hemispheres:
Synaptosome phagocytosis assay and IF staining
Injection of pre-stained synaptosomes
CSF-1R inhibitor
3 x 3.3Gy
Analyze
days after WBRT
-11
0
10
33
36
b
% PSD-95+ Microglia
Sham
WBRT
Sham
WBRT
Control diet
CSF-1R inhibitor
c
Ctrl Sham
Ctrl WBRT
CSF-1R inhibitor Sham
CSF-1R inhibitor WBRT
d
% PSD95+ synaptosomes engulfed by microglia
Sham
WBRT
Sham
WBRT
Control diet
CSF-1R inhibitor
e
C5aR
Relative MFI
Sham
WBRT
Sham
WBRT
Control diet
CSF-1R inhibitor
f
CD68
Relative MFI
Sham
WBRT
Sham
WBRT
Control diet
CSF-1R inhibitor
g
CD107a (Lamp1)
Relative MFI
Sham
WBRT
Sham
WBRT
Control diet
CSF-1R inhibitor

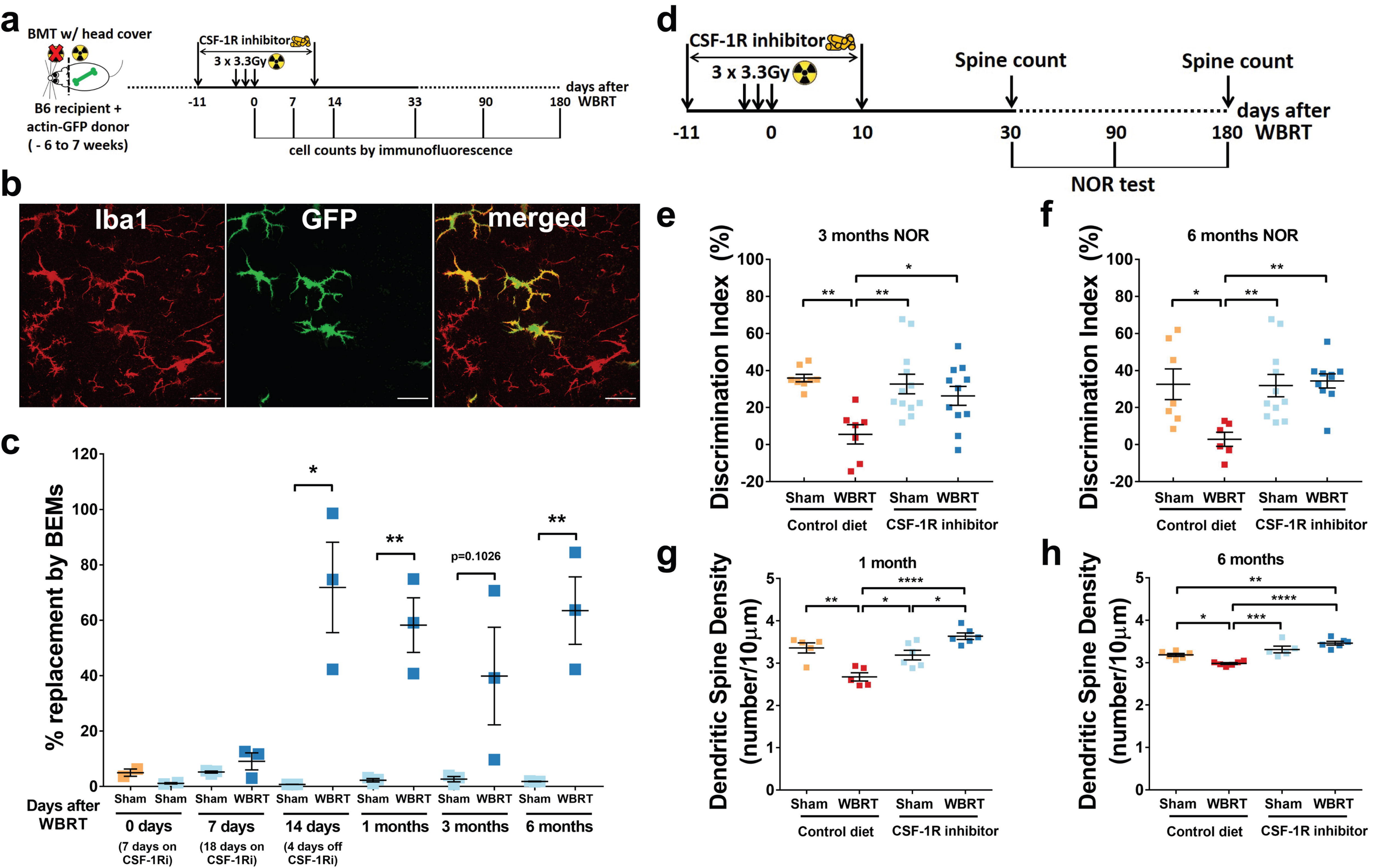
a
BMT w/ head cover
B6 recipient +
actin-GFP donor
(- 6 to 7 weeks)
CSF-1R inhibitor
3 x 3.3Gy
-11
0
7
14
33
90
180
days after WBRT
cell counts by immunofluorescence
b
Iba1
GFP
merged
c
% replacement by BEMs
120
100
80
60
40
20
0
*
**
p=0.1026
**
Sham
Sham
Sham
WBRT
Sham
WBRT
Sham
WBRT
Sham
WBRT
Sham
WBRT
Days after WBRT
0 days
(7 days on CSF-1Ri)
7 days
(18 days on CSF-1Ri)
14 days
(4 days off CSF-1Ri)
1 months
3 months
6 months
d
CSF-1R inhibitor
3 x 3.3Gy
Spine count
Spine count
-11
0
10
30
90
180
days after WBRT
NOR test
e
3 months NOR
Discrimination Index (%)
100
80
60
40
20
0
-20
**
**
*
Sham
WBRT
Sham
WBRT
Control diet
CSF-1R inhibitor
f
6 months NOR
Discrimination Index (%)
100
80
60
40
20
0
-20
*
**
**
Sham
WBRT
Sham
WBRT
Control diet
CSF-1R inhibitor
g
1 month
Dendritic Spine Density (number/10μm)
5
4
3
2
1
0
**
*
*
****
Sham
WBRT
Sham
WBRT
Control diet
CSF-1R inhibitor
h
6 months
Dendritic Spine Density (number/10μm)
5
4
3
2
1
0
*
***
****
**
Sham
WBRT
Sham
WBRT
Control diet
CSF-1R inhibitor